

Nanoscale

Accepted Manuscript



This is an *Accepted Manuscript*, which has been through the Royal Society of Chemistry peer review process and has been accepted for publication.

Accepted Manuscripts are published online shortly after acceptance, before technical editing, formatting and proof reading. Using this free service, authors can make their results available to the community, in citable form, before we publish the edited article. We will replace this *Accepted Manuscript* with the edited and formatted *Advance Article* as soon as it is available.

You can find more information about *Accepted Manuscripts* in the [Information for Authors](#).

Please note that technical editing may introduce minor changes to the text and/or graphics, which may alter content. The journal's standard [Terms & Conditions](#) and the [Ethical guidelines](#) still apply. In no event shall the Royal Society of Chemistry be held responsible for any errors or omissions in this *Accepted Manuscript* or any consequences arising from the use of any information it contains.



Probing individual point defects in graphene via near-field Raman scattering

Received 00th January 20xx,
Accepted 00th January 20xx

DOI: 10.1039/x0xx00000x

www.rsc.org/

Sandro Mignuzzi,^{a,b} Naresh Kumar,^a Barry Brennan,^a Ian S Gilmore,^a David Richards,^b Andrew J. Pollard,^{*a} and Debdulal Roy^{*a}

The Raman scattering D-peak in graphene is spatially localised in close proximity to defects. Here, we demonstrate the capability of tip-enhanced Raman spectroscopy (TERS) to probe individual point defects, even for a graphene layer with an extremely low defect density. This is of practical interest for future graphene electronic devices. The measured TERS spectra enable a direct determination of the average inter-defect distance within the graphene sheet. Analysis of the TERS enhancement factor of the graphene Raman peaks highlights preferential enhancement and symmetry-dependent selectivity of the D-peak intensity caused by zero-dimensional Raman scatterers.

In recent years, considerable research on the vibrational properties of graphene has been performed in the field of Raman spectroscopy¹. A specific effort has been focused on the Raman characterisation of defects within the lattice of graphene and previous works²⁻⁴ have studied the issue of quantifying the level of disorder via Raman spectroscopy. The pioneering work by Tuinstra and Koenig⁵ studied disordered carbon materials and nanocrystalline graphite and reported the presence of a defect-induced Raman peak at $\sim 1340\text{ cm}^{-1}$, now commonly known as the D-peak, which is also present in the Raman spectrum of defective graphene. This was assigned to a breathing mode with A_{1g} symmetry at the K -point of the Brillouin zone, and an inverse proportionality relationship was established between the relative intensity of the Raman D- and G-peak, i.e. $I(D)/I(G)$, and the crystallite lateral size⁵.

The activation of the D-peak is now understood in terms of a double resonance scattering process^{6,7} spatially localised in proximity to a structural symmetry-breaking feature in a graphene sheet, for example an edge^{8,9} or a vacancy defect³. The absorption of the excitation laser generates an electron-hole pair and, if the graphene area exposed to photons contains a defect, electrons can undergo inelastic scattering with a phonon and elastic scattering with the defect, before

recombining and emitting the Raman-scattered photon. Analogous scattering events can involve holes, as well as both electrons and holes⁷. The average length travelled by the electron-hole pair (ℓ) during the whole process delimits the spatial extent of the D-peak activation.

Lucchese *et al.*³ have investigated ion-bombarded graphene by varying the density (n_D) of point defects, or equivalently, the average inter-defect distance, L_D . They proposed a phenomenological expression linking $I(D)/I(G)$ to L_D , as

$$\frac{I(D)}{I(G)} = C_A \frac{(r_A^2 - r_S^2)}{r_A^2 - 2r_S^2} [e^{-\pi r_S^2 / L_D^2} - e^{-\pi(r_A^2 - r_S^2) / L_D^2}] \quad (1)$$

where C_A is the ratio of the relative Raman cross-sections of the D- and the G-peak and is excitation energy dependent, r_S is the radius of the defect and r_A the distance from the centre of the defect for which the D-peak Raman scattering occurs, such that $r_A = r_S + \ell$ (Fig. 1a). We note that a correction factor is needed for $I(D)/I(G)$ when the doping level is not negligible¹⁰, as will be discussed later.

However, there are several issues with conventional confocal Raman spectroscopy when investigating nanoscale defects. Due to the diffraction limit, confocal Raman spectroscopy provides an averaged spectrum over the probe size (typical sizes vary from several hundred nanometres to around $1\ \mu\text{m}^2$ depending on the laser wavelength and numerical aperture), whereas the electron-hole pair involved in the D-peak process is expected to recombine within a few nanometres from the defect^{9,11,12}. Therefore, for typical defect densities it is not possible to spatially resolve individual defects; additionally, inferring the distribution of defects based on the analysis of a confocal Raman spectrum is challenging. Moreover, the confocal Raman spectroscopy signal strength from individual defects is extremely weak, making detection difficult in the case of a very low defect density. Confocal Raman spectroscopy also does not allow a straightforward discrimination among different types of defects when they are present together within the same sample. For example; both vacancies and grain boundaries in chemical vapour deposition (CVD) grown graphene can be regarded as defects, however

^a National Physical Laboratory, Hampton Road, Teddington TW11 0LW, United Kingdom. E-mail: debdulal.roy@npl.co.uk, andrew.pollard@npl.co.uk

^b Department of Physics, King's College London, Strand, London WC2R 2LS, United Kingdom.

they cannot be distinguished and quantified separately using confocal Raman spectroscopy. Specific defects, such as dopant atoms to modify the carrier density of graphene¹³, or sp^3 hybridised bonds in oxidised¹⁴ or fluorinated¹⁵ graphene, can be deliberately introduced rather than being an undesired result of the graphene production process. Hence, knowledge of their distribution is highly desirable to optimise defect engineering in graphene. The quantification of defects in liquid-phase exfoliated graphene using Raman spectroscopy is also particularly challenging¹⁶, as the graphene flake size is comparable to the confocal probe size and the D-peak signal from the edge is therefore always probed in these measurements. Although other techniques such as electron microscopies or scanning tunnelling microscopy (STM) can be used to resolve individual lattice defects to overcome many of these obstacles, they may be destructive or restricted to conductive substrates respectively.

In this communication, we demonstrate the ability to resolve the near-field Raman scattering signal from a point defect in graphene using tip-enhanced Raman spectroscopy (TERS). Using a plasmonically active metal-coated probe, the Raman scattering signal is locally enhanced at the apex of the TERS probe. This enables the acquisition of a chemical map of a graphene flake with nanoscale resolution, far below the diffraction-limited spatial resolution of confocal Raman spectroscopy. The analysis of the measured near-field Raman spectra enables us to directly and non-destructively enumerate defects within the graphene sheet, thus greatly reducing the uncertainty in L_D when compared with its determination using confocal Raman spectroscopy, which is only able to provide an estimate of the average inter-defect distance.

The nanoscale mapping of graphene and carbon nanotubes is an extremely important area of investigation, as shown by the growing number of publications in this area within the last few years, and individual defects in carbon nanotubes have been identified by TERS imaging in Refs. 17 and 18. With respect to carbon nanotubes, these works were focused on dopants¹⁷ or non-specified defective areas generated by the intense optical field present underneath the probe¹⁸. Ref. 19 has shown tip-enhanced Raman D-peak imaging of graphene edges, which may be regarded as line defects, thus highlighting the potential of TERS for nanoscale characterisation of low-dimensional materials. However, as opposed to individual point defects, graphene edges may also be visualised using confocal Raman imaging because of the lack of spatial confinement along the edge direction, which may extend over several microns. The difference between the one-dimensional nature of line defects and the zero-dimensionality of point defects, as will be discussed later, has profound implications on the measured tip-enhanced peak intensity in relation to the experimental parameters used, and most importantly, on the resulting $I(D)/I(G)$ ratio. Nanoscale imaging of defective graphene was also reported by Ref. 20; however, no quantitative analysis was performed on the D-peak enhancement occurring at defective sites as individual point defects were not spatially resolved, and no correlation

between $I(D)/I(G)$ and L_D was explored. Furthermore, the TERS imaging of graphene in Ref. 20 was carried out in gap-mode, i.e. by sandwiching graphene between a metal substrate and a metal probe, which generates an extremely high electromagnetic field enhancement even capable of imaging single molecules. In the present work, we demonstrate that point defects as small as 1.9 nm in radius can be identified and quantified even with AFM-TERS without the use of gap-mode, which often requires opaque metal substrates. In the present work, along with demonstrating the possibility of identifying point defects in graphene using TERS, we wish to highlight that such capability enables precise determination of L_D , not possible in confocal measurements which are affected by large uncertainties, as will be discussed later.

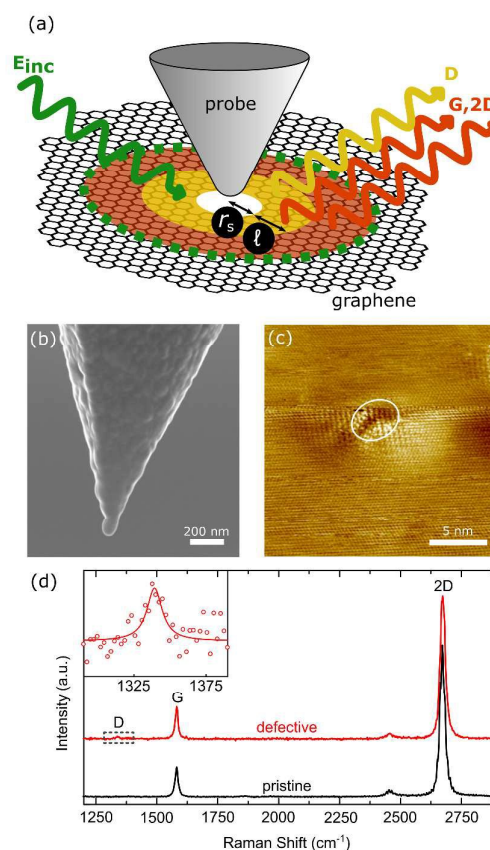


Fig. 1 (a) Schematic diagram of TERS experiment using an Ag-coated AFM probe on a vacancy defect (white disk) in a graphene flake. The incident green light (E_{inc}) illuminates the defect and the TERS probe. The Raman scattering is enhanced from the near-field region (delimited by the green dashed line) where the defect is located. The Raman D-peak scattering occurs in the region around the defect (yellow), whereas the Raman G-peak scattering is present for all areas of the graphene flake that are illuminated (Image not to scale). (b) SEM image of an Ag-coated AFM probe used in this work. (c) STM image of a HOPG surface with a defect (white ellipse) created by bombarding the surface with Bi_3^+ ions (sample voltage 50 mV, tunnel current 1.0 nA). (d) Comparison of the confocal Raman spectrum of pristine and defective graphene. Inset shows the D-peak spectral region in the defective graphene Raman spectrum. Symbols are experimental points and the solid line is a Lorentzian fit.

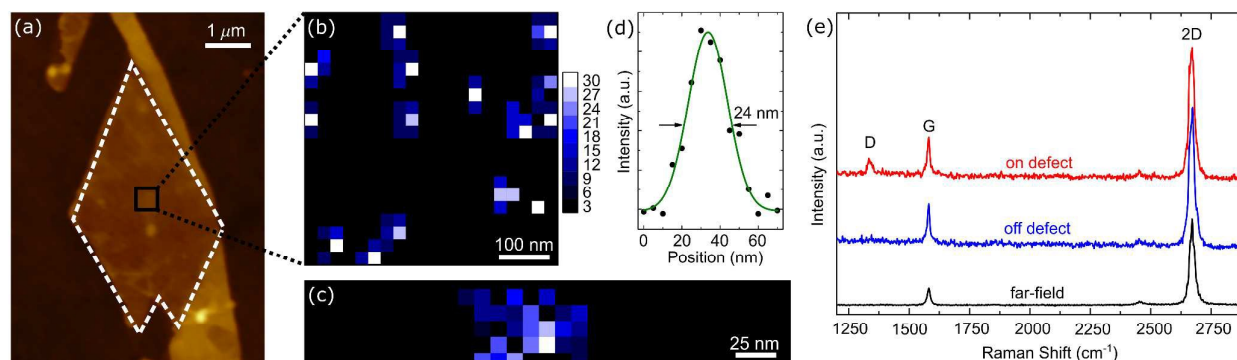


Fig. 2 (a) AFM topography image of a single-layer graphene flake (marked by the white dashed line). (b) TERS map obtained using the Raman D-peak intensity (a.u.), showing the distribution of point defects within the flake. Pixel step-size 25 nm. (c) High resolution TERS image of a point defect obtained using the D-peak intensity. (d) Line profile of the TERS D-peak intensity across a point defect. Dots are experimental points, the solid green line is a Gaussian fit. (e) Comparison of one representative far-field, and two near-field Raman spectra. TERS spectra for when the TERS probe is located at a graphene point defect and when the probe is away from any defects are shown. Integration time per pixel in all TERS data is 5s.

We performed TERS measurements using a transmission-mode system, where the Raman scattered light was collected in a back-scattering geometry, as described in Ref. 21. The sample was illuminated with a 532 nm radially polarised laser using a 100 \times oil-immersion objective lens (NA=1.49). A laser power of < 100 μ W on the sample was used for all measurements. TERS probes were prepared through the thermal evaporation of Ag onto a silicon atomic force microscopy (AFM) cantilever, already covered with an oxide layer (SiO₂) of 300 nm thickness. The probe radius was determined to be \sim 50 nm using scanning electron microscopy (SEM). TERS imaging was performed with the TERS probe in contact with the sample, at an angle of 20 $^\circ$ from the normal to the sample. The laser spot was aligned with the probe apex by progressively moving the objective whilst keeping both the probe and the sample underneath in a fixed position, and by recording the Raman intensity. The maximum Raman intensity is reached when probe and objective are aligned. A schematic of the experiment, along with an SEM image of the TERS probe is shown in Fig. 1.

Graphene samples were produced through mechanical exfoliation of highly oriented pyrolytic graphite (HOPG) on to glass coverslips. A single-layer graphene flake was identified on the substrate through a combination of AFM and confocal Raman spectroscopy. Defects were introduced by means of Bi₃⁺ ion bombardment, with an ion energy of 25 keV, as described in detail in Ref.s 4, 22. These bombardment conditions result in a defect radius of $r_s=1.9\pm 0.1$ nm, as previously determined using STM⁴; an example STM image of a point defect in bombarded HOPG is shown in Fig 1c. The ion current and the exposure time were tuned⁴ to have a defect density of $n_D=10^{10}$ ions/cm², which corresponds to an average inter-defect distance $L_D\cong 100$ nm, according to $L_D=1/\sqrt{n_D}$.

Post-bombardment, a very weak D-peak appears in the confocal Raman spectrum, revealing $I(D)/I(G)=0.03\pm 0.01$ (Fig. 1d). This measurement was performed at the centre of the graphene flake, in order to rule out any contribution of the D-

peak arising from the graphene edges. Based on Eq.1, an $I(D)/I(G)$ value of this order is expected for such a low density of defects. However, due to the uncertainty on the estimated values of C_A , r_s , and ℓ reported in literature^{3, 4}, as well as the uncertainty on the estimated $I(D)/I(G)$ value (arising from the low intensity of the D-peak measured in the Raman spectrum) a precise determination of an average inter-defect distance of this order cannot be obtained using Eq.1. Here we derive from confocal Raman spectroscopy an average inter-defect distance $L_D=100\pm 40$ nm. The large uncertainty in this value results from an application of the worst case uncertainty analysis to Eq.1, where $I(D)/I(G)=0.03\pm 0.01$, as found in this work, and $C_A=5.0\pm 0.9$, $r_s=1.9\pm 0.1$ and $\ell=2.4\pm 0.6$ as reported in Ref. 4, obtained by fitting Eq. 1 to the experimental variation of $I(D)/I(G)$ as a function of L_D .

In general, a scaling factor dependent on the Fermi level energy, E_F , should be taken into account in Eq. 1 whenever doping is introduced¹⁰. The position of the G-peak (Pos(G)), the full width at half maximum (FWHM) of the G-peak (FWHM(G)), the position of the 2D-peak (Pos(2D)), and the intensity ratio between the 2D- and the G-peak, $I(2D)/I(G)$, are sensitive to doping and can subsequently be used to estimate E_F ²³. The Raman spectrum of the graphene flake here investigated shows Pos(G) $\cong 1581$ cm⁻¹, FWHM(G) $\cong 14$ cm⁻¹, Pos(2D) $\cong 2670$ cm⁻¹, $I(2D)/I(G)\cong 4.8$, that are consistent with negligible doping ($E_F<100$ meV). Such doping occurs naturally upon exfoliation, due to a combination of surface adsorbates after exposure of the graphene flake to ambient conditions²⁴, and of charge transfer with the substrate²⁵. These values do not vary significantly when defects are introduced and therefore no renormalisation is needed.

Fig. 2b shows a TERS D-peak map (500 \times 500 nm²) of the defective graphene flake shown in Fig. 2a, and a high-resolution map of an individual defect is shown in Fig. 2c. From visual inspection of Fig. 2b and the representative Raman spectra (red and blue lines in Fig. 2e) extracted from this TERS map, it is evident that $I(D)$ is distinctly more intense

$I(D)/I(G) \cong 0.3$) where point defects are located. For these points, the FWHM of the D-peak is $\sim 20 \text{ cm}^{-1}$, consistent with the low disorder regime². From the same TERS data, $I(D)$ is shown to be negligible and below the noise level for non-defective areas of the graphene flake. We do not observe any commensurate change in the intensities or FWHM of the G- and 2D-peaks, which are uniform over the scanned area.

The ability to visualise the Raman scattering from each point defect enables a direct quantitative analysis. This is particularly important for very low defect densities, where the value of L_D becomes comparable to the confocal Raman probe size, and the associated error of L_D , when determined using Eq. 1, increases significantly. However, from Fig. 2b, we directly observe that the inferred value of $L_D \cong 100 \text{ nm}$ determined from the ion bombardment is consistent with the distribution of individual defects revealed using TERS imaging, from which we determine $L_D \cong 130 \text{ nm}$.

We note that Ref. 18 suggested a different model for assessment of L_D based on $I(D)/I(G)$ in carbon nanotubes, i.e. the relationship $I(D)/I(G) \propto 0.5 \text{ nm} \times 1/L_D$. However, as Ref. 18 could not spatially resolve point defects they could not provide a quantitative comparison between the confocal $I(D)/I(G)$ and the number of defects, as has been presented here. In addition to this, the present analysis allows us to compare the different enhancement of the D- and G-peaks (as will be shown later), which was neglected in the model suggested by Ref. 18.

A TERS map of a given Raman peak is always the convolution of the spatial distribution of the Raman scattering signal itself with the spatial extent of the region where the field enhancement takes place, which corresponds to the TERS spatial resolution. In the case of an effective zero-dimensional object, such as a point defect, the line-profile essentially corresponds to the spatial resolution of the TERS probe, which in this case is $\sim 24 \text{ nm}$ (Fig. 2d). To resolve the shape of the ring associated to the D-peak (shown as a yellow area in Fig. 1a) the spatial resolution must be much improved (down to 1–2 nm). This resolution has been demonstrated in particular experimental conditions such as cryogenic temperature, ultra-high vacuum²⁶ or STM-based TERS²⁷, where a conductive substrate is required. However, our TERS measurements are conducted without any environmental constraint.

In order to compare the confocal and tip-enhanced Raman spectra we introduce the following concepts. In a tip-enhanced Raman spectrum, the peak intensities represent the sum of two Raman scattering contributions arising from the near-field enhancement region and from the region illuminated by the confocal probe, i.e. the far-field. We define the enhancement factor (η)²⁸ as

$$\eta = \alpha \frac{I_{\text{NF}}}{I_{\text{FF}}} \quad (2)$$

where NF and FF stand for near-field and far-field respectively. I_{NF} and I_{FF} are the peak intensities, with the ratio $I_{\text{NF}}/I_{\text{FF}}$ usually referred to as *contrast*²¹. The value of η for the G- and 2D-peaks can be calculated using Eq. 2 through consideration of A_{NF} and A_{FF} , the areas of the sample that produce the

particular Raman scattering peak under investigation, such that $\alpha = A_{\text{FF}}/A_{\text{NF}}$.

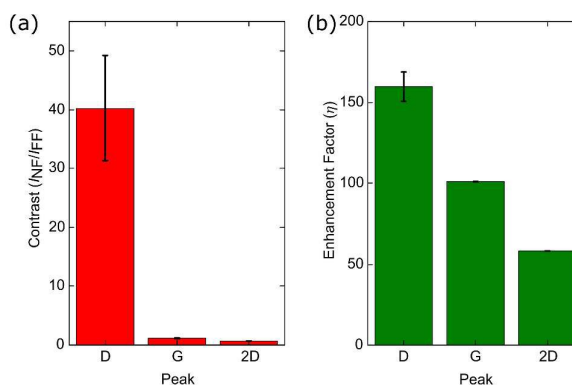


Fig. 3 (a) Contrast and (b) enhancement factor for the main Raman scattering peaks. Error bars represent the standard error from the fitting process. The contrast for the D-peak depends on the number of defects probed within the far-field area, equal to α .

The G- and 2D-peaks are allowed Raman modes arising from the whole of the probed graphene area. Therefore A_{NF} and A_{FF} are calculated for these peaks using the near-field and far-field spatial resolutions respectively, where A_{FF} is determined using a diameter of the confocal probe of 225 nm^2 , and A_{NF} is determined using the near-field spatial resolution previously calculated from Fig. 2d. Contrarily, D-peak Raman scattering is localised close to defects and therefore, for a spatial resolution greater than $2r_A$, $\alpha = n_D \times A_{\text{FF}}$, that is the number of defects within the probed far-field area. Here, $\alpha \cong 4$ for $L_D = 100 \text{ nm}$.

The values of the enhancement factor η and the calculated contrasts of the D-, G- and 2D-peaks are summarised in Fig. 3. The contrast of the D-peak is ~ 40 times higher in comparison to the G- and 2D-peaks, mainly due to the high localisation of the D-peak around the defects and the very low number of defects probed within the far-field area.

The analysis of the enhancement factor is far from trivial as it depends on several factors^{29–32}, such as the probe-sample distance, the incident laser polarisation, the angle of the probe to the sample normal, the symmetry of the modes, the dimensionality of the Raman scatterer, the coherence of the Raman scattering and the plasmonic resonant profile of the probe.

In particular, we note that the enhancement factor of the G-peak is ~ 1.5 times lower than that of the D-peak. This is expected when the spatial resolution is less than the coherence length of the phonons, i.e. $\cong 30 \text{ nm}$ for optical phonons in graphene³¹. In the fully coherent regime, the intensity of the G-peak from the near-field region should in principle vanish due to destructive interference effects³¹ arising from the particular symmetry of the mode (E_{2g}), for a polarisation that is perpendicular to the sample. However, we still observe an enhancement for the G-peak due to a probe angle, and hence polarisation directly beneath the probe, of 20° to the sample normal (note that, in addition, the probe dipole angle is generally randomly oriented). As the symmetry of the D-peak is assigned to the A_{1g} symmetry, the

corresponding signals from the near-field region add in-phase³¹. However, we note that in this case the D-peak is heavily enhanced due to the fact that the defect acts as a zero-dimensional point source, i.e. a steeper D-peak signal increase is expected as the probe approaches the sample³¹. Although the 2D-peak shares the same A_{1g} symmetry, we observe a much lower enhancement factor compared to both the D- and the G-peaks. This observation may be due to the variation of the plasmonic resonant profile of the silver-coated TERS probe, leading to a different scale of enhancement for the 2D-peak, as the associated Raman shift ($\sim 2670\text{ cm}^{-1}$) is much higher than that of the D- and G-peaks. This effect is particularly relevant for Ag-coated probes, as Ag exhibits much sharper resonances^{33, 34} when compared to Au³⁵, which is also frequently used for TERS measurements.

We note that the probe position, relative to the sample and the laser focus, could affect the calculation of contrast and enhancement factor using Eq. 2 (as mentioned above). This effect can be separated in two contributions: the movement of the probe in the plane of the sample, affecting the tip-laser alignment, and the movement of the probe in the direction perpendicular to the sample. In the plane of the sample, the probe is placed within the confocal probe diameter of 225 nm, corresponding to the FWHM of its Gaussian spatial intensity profile, such that TERS enhancement has a very weak dependence on any small misalignment between the probe and the laser focus. On the other hand, in the direction perpendicular to the sample, the probe position is governed by the AFM feedback control. As this is much less than the radius of curvature of the probe, the enhancement factor is not expected to be affected.

Ref. 32 reports on a theoretical study of the enhancement factors for graphene's most prominent Raman peaks, occurring in proximity to a *one*-dimensional scattering site. The authors predicted a symmetry-dependent enhancement of the D-peak, which was experimentally validated later in Ref. 31 via a TERS scan across a graphene edge. A similar qualitative selectivity – albeit with a different numerical value of enhancement factor – should in principle be observed for a lower dimensionality scatterer. To the best of our knowledge, our observed preferential enhancement of the D-peak at a point defect site constitutes the first experimental validation of the selective D-peak enhancement in *zero*-dimensional sources.

Conclusions

In conclusion, we have investigated the near-field Raman scattering arising from individual point defects in graphene. We have demonstrated for the first time that, by overcoming the diffraction limit of confocal Raman spectroscopy, tip-enhanced Raman spectroscopy enables detection of highly localised defects in graphene via their D-peak, with a resolution of $\sim 24\text{ nm}$. We have shown that a near-field Raman map allows a direct assessment of the amount and distribution of point defects within the probed graphene area, thus

overcoming the large uncertainty in the average inter-defect distance when determined using confocal Raman spectroscopy. The analysis of contrast and enhancement factors evaluated in proximity to a point defect has highlighted a selective, symmetry-dependent enhancement of the D-peak intensity at a zero-dimensional site, thus experimentally validating available theoretical predictions.

Through the understanding gained via Raman spectroscopy measurements at the nanoscale, the effect of disorder on conventional confocal Raman spectroscopy measurements, which is predicted to be the technique of choice for graphene quality control, can be better understood. This work paves the way towards the nanoscale, and non-destructive investigation of individual defects in graphene-based devices and other two-dimensional materials^{22, 36}. This is particularly important as electronic device dimensions are constantly being reduced (down to the few nanometre scale), so the need to probe point defects, which could have an enormous impact on device performances, will be essential.

Acknowledgements

This work forms part of the Graphene project (No.s 115948 and 118616) in the Innovation R&D programme and Raman Metrology project (No. 116326) in the Chemical and Biological programme of the National Measurement System of the U.K. Department of Business, Innovation and Skills and with funding by the European Metrology Research Programme (EMRP) Project NEW02: Raman Metrology. The EMRP is jointly funded by the EMRP participating countries within EURAMET and the European Union. The authors would like to thank Dr Nicola Bonini for discussions related to the manuscript.

Notes and references

- 1 A. C. Ferrari and D. M. Basko, *Nat. Nanotechnol.*, 2013, **8**, 235-246.
- 2 L. G. Cançado, A. Jorio, E. H. M. Ferreira, F. Stavale, C. A. Achete, R. B. Capaz, M. V. O. Moutinho, A. Lombardo, T. S. Kulmala and A. C. Ferrari, *Nano Lett.*, 2011, **11**, 3190-3196.
- 3 M. M. Lucchese, F. Stavale, E. H. M. Ferreira, C. Vilani, M. V. O. Moutinho, R. B. Capaz, C. A. Achete and A. Jorio, *Carbon*, 2010, **48**, 1592-1597.
- 4 A. J. Pollard, B. Brennan, H. Stec, B. J. Tyler, M. P. Seah, I. S. Gilmore and D. Roy, *Appl. Phys. Lett.*, 2014, **105**, 253107.
- 5 F. Tuinstra and J. L. Koenig, *J. Chem. Phys.*, 1970, **53**, 1126-1130.
- 6 C. Thomsen and S. Reich, *Phys. Rev. Lett.*, 2000, **85**, 5214-5217.
- 7 P. Venezuela, M. Lazzeri and F. Mauri, *Phys. Rev. B*, 2011, **84**, 035433.
- 8 L. Cançado, M. A. Pimenta, B. Neves, M. Dantas and A. Jorio, *Phys. Rev. Lett.*, 2004, **93**, 247401.
- 9 C. Casiraghi, A. Hartschuh, H. Qian, S. Piscanec, C. Georgi, A. Fasoli, K. S. Novoselov, D. M. Basko and A. C. Ferrari, *Nano Lett.*, 2009, **9**, 1433-1441.
- 10 M. Bruna, A. K. Ott, M. Ija, D. Yoon, U. Sassi, A. C. Ferrari and M. Ijas, *ACS Nano*, 2014, **8**, 7432-7441.
- 11 D. Basko, *Phys. Rev. B*, 2009, **79**, 205428.

- 12 R. Beams, L. G. Cançado and L. Novotny, *Nano Lett.*, 2011, **11**, 1177-1181.
- 13 H. Wang, Q. Wang, Y. Cheng, K. Li, Y. Yao, Q. Zhang, C. Dong, P. Wang, U. Schwingenschlogl, W. Yang and X. X. Zhang, *Nano Lett.*, 2012, **12**, 141-144.
- 14 R. K. Joshi, P. Carbone, F. C. Wang, V. G. Kravets, Y. Su, I. V. Grigorieva, H. A. Wu, A. K. Geim and R. R. Nair, *Science*, 2014, **343**, 752-754.
- 15 F. Withers, M. Dubois and A. K. Savchenko, *Phys. Rev. B*, 2010, **82**, 1-4.
- 16 K. R. Paton, E. Varrla, C. Backes, R. J. Smith, U. Khan, A. O'Neill, C. Boland, M. Lotya, O. M. Istrate, P. King, T. Higgins, S. Barwich, P. May, P. Puczkarski, I. Ahmed, M. Moebius, H. Pettersson, E. Long, J. Coelho, S. E. O'Brien, E. K. McGuire, B. M. Sanchez, G. S. Duesberg, N. McEvoy, T. J. Pennycook, C. Downing, A. Crossley, V. Nicolosi and J. N. Coleman, *Nat. Mater.*, 2014, **13**, 624-630.
- 17 I. O. Maciel, N. Anderson, M. A. Pimenta, A. Hartschuh, H. Qian, M. Terrones, H. Terrones, J. Campos-Delgado, A. M. Rao, L. Novotny and A. Jorio, *Nat. Mater.*, 2008, **7**, 878-883.
- 18 C. Georgi and A. Hartschuh, *Appl. Phys. Lett.*, 2010, **97**, 143117.
- 19 W. Su and D. Roy, *J. Vac. Sci. Technol. B*, 2013, **31**, 041808.
- 20 J. Stadler, T. Schmid and R. Zenobi, *ACS Nano*, 2011, **5**, 8442-8448.
- 21 N. Kumar, A. Rae and D. Roy, *Appl. Phys. Lett.*, 2014, **104**, 123106.
- 22 S. Mignuzzi, A. J. Pollard, N. Bonini, B. Brennan, I. S. Gilmore, M. A. Pimenta, D. Richards and D. Roy, *Phys. Rev. B*, 2015, **91**, 195411.
- 23 A. Das, S. Pisana, B. Chakraborty, S. Piscanec, S. K. Saha, U. V. Waghmare, K. S. Novoselov, H. R. Krishnamurthy, A. K. Geim, A. C. Ferrari and A. K. Sood, *Nat. Nanotechnol.*, 2008, **3**, 210-215.
- 24 F. Schedin, A. K. Geim, S. V. Morozov, E. W. Hill, P. Blake, M. I. Katsnelson and K. S. Novoselov, *Nat. Mater.*, 2007, **6**, 652-655.
- 25 Y. Shi, X. Dong, P. Chen, J. Wang and L. J. Li, *Phys. Rev. B*, 2009, **79**, 1-4.
- 26 R. Zhang, Y. Zhang, Z. C. Dong, S. Jiang, C. Zhang, L. G. Chen, L. Zhang, Y. Liao, J. Aizpurua, Y. Luo, J. L. Yang and J. G. Hou, *Nature*, 2013, **498**, 82-86.
- 27 C. Chen, N. Hayazawa and S. Kawata, *Nat. Commun.*, 2014, **5**, 3312.
- 28 N. Kumar, S. Mignuzzi, W. Su and D. Roy, *EPJ Tech. Instrum.*, 2015, **2**, 9.
- 29 L. Cançado, A. Jorio, A. Ismach, E. Joselevich, A. Hartschuh and L. Novotny, *Phys. Rev. Lett.*, 2009, **103**, 186101.
- 30 R. V. Maximiano, R. Beams, L. Novotny, A. Jorio and L. G. Cançado, *Phys. Rev. B*, 2012, **85**, 235434.
- 31 R. Beams, L. G. Cançado, S.-H. Oh, A. Jorio and L. Novotny, *Phys. Rev. Lett.*, 2014, **113**, 186101.
- 32 L. G. Cançado, R. Beams, A. Jorio and L. Novotny, *Phys. Rev. X*, 2014, **4**, 031054.
- 33 F. Demming, J. Jersch, K. Dickmann and P. I. Geshev, *Appl. Phys. B*, 1998, **66**, 593-598.
- 34 P. I. Geshev, S. Klein, T. Witting, K. Dickmann and M. Hietschold, *Phys. Rev. B*, 2004, **70**, 075402.
- 35 C. Sönnichsen, S. Geier, N. E. Hecker, G. von Plessen, J. Feldmann, H. Ditlbacher, B. Lamprecht, J. R. Krenn, F. R. Aussenegg, V. Z.-H. Chan, J. P. Spatz, M. Möller, C. Sönnichsen and M. Möller, *Appl. Phys. Lett.*, 2000, **77**, 2949-2951.
- 36 A. J. Pollard, N. Kumar, A. Rae, S. Mignuzzi, W. Su and D. Roy, *J. Mater. Nanosci.*, 2014, **1**, 39-49.